Computers and Structures 276 (2023) 106955

Contents lists available at ScienceDirect

Computers and Structures

journal homepage: www.elsevier.com/locate/compstruc

Design and fabrication of artificial brain coral: Evolution principle, turbulent hydrodynamics and matter interchange

Sen Lin [a,*], Nengzhuo Chou [a], Dingwen Bao [b,c], Genbao Zhang [d], Chengwang Xiong [e], Jie Fang [f], Yi Min Xie [b]

[a] *State Key Laboratory of Advanced Design and Manufacturing for Vehicle Body, College of Mechanical and Vehicle Engineering, Hunan University, Changsha 410082, China*
[b] *Centre for Innovative Structures and Materials, School of Engineering, RMIT University, GPO Box 2476, Melbourne 3001, Australia*
[c] *School of Architecture and Urban Design, RMIT University, GPO Box 2476, Melbourne 3001, Australia*
[d] *College of Civil Engineering, Hunan City University, Yiyang, Hunan 413000, China*
[e] *College of Shipbuilding Engineering, Harbin Engineering University, Harbin 150001, China*
[f] *Beijing Institute of Control and Electronic Technology, Beijing 102308, China*

ARTICLE INFO

Article history:
Received 30 June 2022
Accepted 1 December 2022

Keywords:
Brain corals
Topological optimization
Turbulent hydrodynamics
Matter interchange

ABSTRACT

This paper presents a study of the morphogenesis of brain corals based on an experimental investigation and a topological optimization method. The resistance to matter interchange was employed to allocate the optimal space for the growth of polyp colonies from the perspective of topological optimization, where the optimized structures are those of natural brain corals. Computational fluid dynamics simulations revealed that these complicated structures can provide shelter to protect polyps from ocean currents. A reverse mold was prepared from silica gel and used to cast models from mixtures of cement and calcium carbonate, where the mixture ratio was determined based on compressive strength and biocompatibility. Based on an acid corrosion experiment, the matter interchange capability was verified. This study also proved that the many folds in the structure of brain corals contribute to the circulation of seawater, thus maintaining the concentration of nutrients and hindering the deposition of harmful substances. This paper establishes an innovative methodology for the creation of artificial brain corals, which is important for environmental restoration.

1. Introduction

In recent decades, coral aquaculture techniques have been under development in many countries to support the conservation of endangered natural coral reefs in the face of an increasing live coral market [1]. Such techniques could provide an effective means of restoring coral reefs [2], which are declining worldwide due to human impacts such as pollution [3], fishing [4], coastal development [5], and climate change [6]. Industries that specialize in the production of artificial reefs often use reinforced concrete structures to assist in coral reproduction [7]. Accordingly, these artificial reefs can generally be defined as man-made structures placed underwater to mimic certain characteristics of natural reefs [8].

The potential of community-based coral aquaculture has been evaluated from various perspectives in recent years. In Madagascar, researchers investigated suitable farming techniques using the species *Acropora nasuta* and *Seriatopora caliendrum* [9]. In their studies, the survival and growth rates of the nubbins during wet/warm and dry/cold seasons were compared. Similarly, a significant variation in growth rate has been observed between naturally recruited and transplanted corals during the monsoon period [10].

As an emerging class of techniques, advanced manufacturing [11] has enabled researchers to produce man-made experimental models that can serve as structural replicates of or specifically manipulated alternatives to natural habitats in order to study the behaviors and habitat preferences of aquatic species [12]. For instance, the interstitial space of a 3D printed oyster reef has been quantitatively manipulated to gain an understanding of the structural properties that mediate the foraging success of *Callinectes sapidus* [13]. Moreover, 3D-printed reefs have natural surface pH values that are favorable for the growth of coral larvae. With the assistance of 3D printing techniques, it is possible to mimic the natural complexity (caves and connecting tunnels) of coral reefs and enhance the diversity of artificial reefs [14]. Although 3D printing has the potential to advance efforts to protect coral reefs, the immaturity of some relevant technologies may seriously limit the application prospects of this advanced concept [15]. One important reason is that engineers tend to simply imitate the shape of corals [16] or use engineering methods to design artificial coral reefs [17] that are not consistent with the growth principle of corals [18].

---

[*] Corresponding author.
E-mail address: senlin@hnu.edu.cn (S. Lin).

https://doi.org/10.1016/j.compstruc.2022.106955
0045-7949/

Another aspect of additive manufacturing that is of concern to oceanologists is that the printing materials used must meet certain manufacturability requirements. Consequently, most objects are fabricated in plastic, which is incompatible with colonization by marine organisms [19]. Instead, nontoxic composites such as cementitious mixtures of biological bone would be more suitable for printing artificial marine constructions [20].

Interdisciplinary efforts offer further possibilities; in particular, many researchers have attempted to employ topological optimization methods to analyze the features of biological structures [21] for subsequent application [22]. The precondition for such application is that scholars in topological optimization have proven that the dependence of the objective function on the design variables can be incorporated into structural designs using the adjoint technique [23]. Furthermore, methods for solving partial differential equations using artificial neural networks [24] or deep neural networks (DNNs) [25] have been proposed. Optimal heat conduction paths have been designed by using a novel topological optimization method [26]. The complexity of a structure is usually characterized in terms of the geometries of the interior holes, which can be well controlled based on graph theory [27]. Additionally, the bidirectional evolutionary structural optimization (BESO) algorithm has been verified as an effective means of explaining the hollow sectional structures of aquatic plants [28]. Recently, a new topological optimization method for designing workpieces with lightweight structures and acceptable mechanical strength has been proposed for generating bioinspired porosities based on bones of various shapes, sizes and orientations [29]. More recently, human-made corals have been developed by minimizing a carbon-solidification-related objective function and considering the morphological characteristics of staghorn corals [30].

Regarding the turbulent hydrodynamics of corals, the complex structures of these marine habitats influence wave activity, which appears to enhance the rates of mass transport in the water surrounding corals [31]. For instance, strong bottom currents play a key role in cold-water coral environments by shaping their morphology and providing the necessary food for the corals to thrive [32]. This interesting phenomenon has motivated researchers to employ fluid mechanics methods to investigate it [33]. The effects of reef permeability on the spatial distributions of the wave-induced currents inside and outside an inhomogeneous coral reef body have been studied using an improved weakly compressible smoothed particle hydrodynamic mixture model [34]. Such research can serve as a crucial reference for differential survivorship during heat-induced coral bleaching, particularly as thermal stress events become increasingly common due to global climate change [35].

The rest of this paper is organized as follows. Section 2 introduces how the resistance to matter interchange in the projected surface domain was set as the objective for topological optimization under volume and length constraints. As described in Section 3, computational fluid dynamics (CFD) simulations were then implemented to investigate the characteristics of the flow field around these human-made corals. Section 4 reports an experimental investigation in which a silica gel reverse mold was prepared for casting models in cement and calcium carbonate, where the mixture ratio was determined based on tests of workability and compressive strength. An acid corrosion test was conducted to verify the matter interchange capability of the optimized morphology. The proposed methodology is intended to facilitate the creation of artificial brain corals, which is important for environmental restoration.

2. Methodology

2.1. Aquatic observation

As a kind of reef-building coral, brain corals live in tropical sea water at latitudes below 19°. They tend to reproduce in shallow water with sufficient illumination. The samples of *Platygyra*, *Goniastrea* and *Lobophyllia* (approximately 0.03–0.10 m in dimension) studied here were collected from the seabed near Lizard Island, Australia (14°40′37″ S, 145°26′17″ E; shown in Fig. 1a), and were subsequently observed for 10 months (Fig. 1b,c&d).

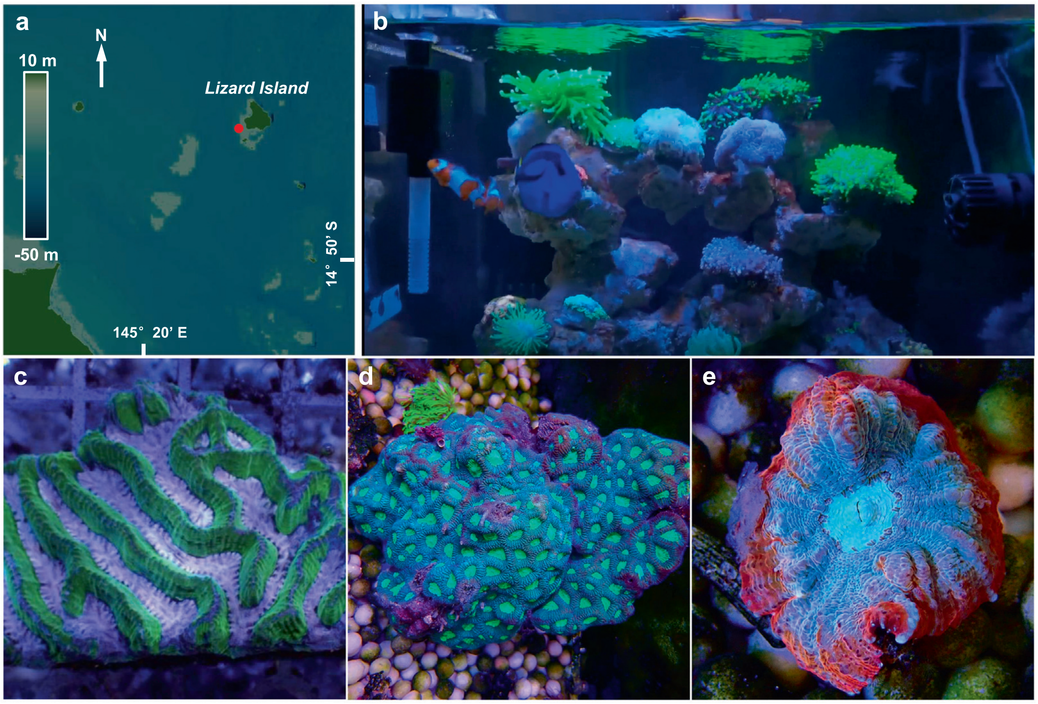

Fig. 1. The sample collection site and the appearances of samples: (a) the elevation data (from the National Geophysical Data Center (NGDC)) near the site; (b) a panoramic view of the mariculture chamber; (c) the appearance of *Platygyra*; (d) the appearance of *Goniastrea*; (e) the appearance of *Lobophyllia* (b–e were photographed by N.Z. Chou).

In the sea water used to cultivate brain corals, sufficient calcium is crucial to ensure the healthy growth of their internal skeletons. In contrast, it is better to limit the levels of NO_3^- and PO_4^{3-}, as high concentrations of these chemicals can cause polyps to become necrotic. Brain corals are well suited for living in moderate water flows. When exposed to swift currents, however, they often contract, which is likely to cause tissue damage. Another key factor in brain coral feeding is light; specifically, medium or bright light is appropriate. Nevertheless, a freshly transplanted coral should not be exposed to strong light immediately. It is suggested that it be placed in a deep and dark location, where its position can be gradually raised to permit adaptation to stronger light.

In this study, an experimental chamber (0.80 m×0.50 m×0.80 m) made of polymethyl methacrylate was employed for mariculture purposes, in which the current speed was controlled between 1500 and 2000 gph by an MP10wQD propeller pump (EcoTech Marine Inc., United States) and a Seio 620 circulation propeller pump (Zhongshan SOBO Electric Co., Ltd., China). The salinity was controlled between 3.45% and 3.55% (mean = 3.50%). The water temperature ranged from 24.1 °C to 26.5 °C and was regulated by an HC-2200BH water temperature control machine (Shenzhen HaiLea Tech. Co., Ltd., China). The stability of the primary nutrients was maintained within reasonable limits by means of a smart dosing pump (Wavereef Aquarium Co., Ltd., China), with the concentrations of Ca2+, NO_3^- and PO_4^{3-} being 400, 12.5 and 0.02, respectively. The pH value was stabilized in the range of 8.1–8.4, as measured by an Orion Star A121 portable pH meter (Thermo Fisher Scientific Inc., United States). Artificial light was maintained for 10–18 h every day with a Radion XR30w G4 light fixture (EcoTech Marine Inc., United States). For water purification, an AE-DF130 protein skimmer (Guangzhou Kas Aquarium Equipment Manufacturing, Germany) was used.

2.2. Topological optimization

Like most reef-building corals, once the larvae of brain corals have chosen a place to settle, they remain stationary throughout their lives and grow on reef ridges. Being symbiotic with zooxanthellae, these animals use photosynthesis from symbiotic algae to create organic matter for growth, and they also use their stinging tentacles to capture plankton from the water. Therefore, the living spaces of brain corals, which are home to competition among polyps on the same individual, are significant for investigating the formation of their shapes. In this case, the problem can be regarded as the optimal design of a space-occupying configuration. The distribution of the polyps on a domed colony can be simplified to a design 'density' variable ρ on a 2-D domain with an irregular shape, where low values represent the 'valleys' of the polyps, which serve a predation function, while high values represent the 'ridges' of the polyps, which play a protective or partitioning role. The coefficient of matter interchange, $k(\rho)$, corresponds to the living spaces of the polyps. The solid isotropic material with penalization (SIMP) method was employed here for topological optimization to ensure robust topological development and convincing physical validation. Notably, the SIMP method comprises abundant subalgorithms involving size constraints and mesh independence. The interchange of matter between brain coral and nearby seawater can be regarded as the distribution and exchange of organics between polyps with strong metabolic activity and essential nutrients in the seawater. In particular, the interchange activity associated with convective water flow occurs mainly at the interface between the coral and the seawater. The formulation of a suitable objective function for such a matter (or heat) transfer optimization problem has been a topic of discussion for a long time [36]. It has been found that minimizing the compliance of matter (heat) can usually lead to a desirable structure with better comprehensive properties compared with directly minimizing the matter concentration (temperature) in the design domain. Accordingly, the objective function for matter interchange, f_m, can be defined to minimize the matter interchange resistance of the design domain Ω by means of an optimized material distribution ρ:

$$\begin{aligned} &min: f_m = \int_\Omega (\nabla[k(\rho)\nabla T] - \mathbb{C}) T d\Omega \\ &s.t. \begin{cases} \int_\Omega \rho d\Omega \leqslant V^* \\ \rho_{min} \leqslant \rho \leqslant 1 \\ \nabla[k(\rho)\nabla T] - \mathbb{C} = \mathbf{C} \end{cases} \end{aligned} \tag{1}$$

where $T(x, y)$ is the growing matter content in the coral, x and y are two-dimensional coordinates, and V^* is an upper-bound limit on the allowable solid part volume fraction. In a confined domain, the mouth part of a coral structure can increase the efficiency of matter interchange, while the ridges can influence the direction of water flow to carry away waste. Therefore, the polyps must be properly proportionately allocated between the mouth and ridges. A corresponding volume constraint can be set based on biological characteristics ($V^* \approx 0.5$, obtained from aquatic observations). $\rho_{min} \approx 0.1$ is the minimum density of the coral, which is generally measured from the density ratio between the valleys and ridges. $\mathbb{C}$ is matter interchange on the surface of the coral, and $\mathbf{C}$ is the production of matters in the polyps. Regarding numerical implementation, in this work, the above 2-D conduction topology optimization problem has been extended to consider side-surface convection, with the added benefit of design in two dimensions. The incorporation of side-surface convection into the design problem leads to the following governing equation for the objective function:

$$\mathbb{C} = s(\rho)(T - T_0) \tag{2}$$

where $s(\rho)$ represents the design-dependent side-surface convection coefficient at a reference matter content of T_0. In addition, the coefficient of matter interchange can be interpolated as follows:

$$k(\rho) = [\sigma + (1 - \sigma)\rho^p]k_0 \tag{3}$$

where $p \geqslant 3$ is a penalty parameter, k_0 is a reference value for the matter interchange coefficient of the polyps (including their zooxanthellae), and σ represents the ratio of matter interchange between the ridges/seawater and the valleys of the polyps, which should be very small (10^{-3}). Moreover, the side-surface convection coefficient $s(\rho)$ in Eq. 2 is specified by a simplified hat function:

$$s(\rho) = \begin{cases} 0.01s_0, & \rho_l \leqslant \rho < \rho_u \\ s_0, & \rho_{min} \leqslant \rho < \rho_l \\ 0, & \rho_u \leqslant \rho \leqslant 1 \end{cases} \tag{4}$$

where s_0 is the reference full-magnitude convective matter interchange coefficient defined at the external surface of the coral and ρ_l and ρ_u are lower and upper cutoff values, respectively, for the side-surface convection coefficient. At the valley-to-seawater interfaces ($\rho_{min} \leqslant \rho < \rho_l$), where the side-surface convection coefficient takes its full-magnitude value, matter interchange activities occur most frequently. Meanwhile, because of the many cavities, the density value here is relatively low ($\rho \approx 0.1$, based on specimen estimation). On the ridges ($\rho_l \leqslant \rho < \rho_u$), the side-surface convection coefficient turns out to be a small fraction of s_0 due to relative metabolic inactivity. Furthermore, the inner parts of the coral ($\rho_u \leqslant \rho \leqslant 1$) are skeletons, where the side-surface convection coefficient is 0. Finally, the lower cutoff value should be defined as the maximum valley density, $\rho_l \approx 0.5$, while the upper cutoff value should be set to the surface density on ridges, $\rho_u \approx 0.9$. Predictably, because of the high matter exchange efficiency in the valleys, the corals will evolve toward a more sinuous mouth. In the case of ridges, a large size or a concentrated distribution would reduce metabolic activity; thus, slender ridges are preferred for brain corals.

In the described example and most of the literature referenced above, a primary challenge facing the implementation of brain-like patterns is the thickness of the ridges and valleys. This is because wrinkles that are too large or small are rare due to their biological nature. Therefore, a length-scale constraint for controlling the thickness of the wrinkles is introduced here [37]. Suppose that the average density in the vicinity of element i is expressed as

$$\widetilde{\rho}_i = \left(\sum_{j\in\Omega_i} v_j\right)^{-1} \sum_{j\in\Omega_i} v_j \rho_j^{\xi} \tag{5}$$

where Ω_i denotes the element design domain for elements located in a circle centered at element i, v_j represents the area of each element included in the domain Ω_i, and the exponent $\xi = 0.5$ acts as a density amplifier. A smaller value of the parameter ξ indicates that an element with an intermediate density value ($0 < \rho_j < 1$) is more likely to be counted as a solid element (e.g., for $\rho_j = 0.7, \rho_j^{\xi} = 0.84$ with $\xi = 0.5$, while $\rho_j^{\xi} = 0.90$ with $\xi = 0.3$). In this case, the length-scale constraint that describes the biological features of corals is imposed by minimizing the objective function

$$min : f_l = \sum_{j\in\Omega_i} max(0, \widetilde{\rho}_i - \gamma) \tag{6}$$

where $0 < \gamma < 1$ is the upper area fraction ratio in the length-scale domain Ω_i of element i. When $\gamma$is given a certain value, e.g., 0.95, the volume fraction in Ω_i will not exceed that value. The sensitivity of the length-scale constraint can be expressed as $\partial f_l/\partial\rho = \sum_{j\in\Omega_i} max(0, \widetilde{\rho}_i/\partial\rho)$. By removing the constant, the sensitivity expression can be further simplified to

$$\frac{\partial f_l}{\partial\rho} = \frac{1}{\xi v_i}\partial f_l/\partial\rho = \rho_i^{\xi-1}\sum_{j\in\Omega_i}(\beta_j/v_j) \tag{7}$$

where β is related to the Heaviside function in topological optimization [37] and can be simplified to

$$\beta_j = \begin{cases} 1, & \widetilde{\rho}_i > \gamma \\ 0, & \widetilde{\rho}_i \leqslant \gamma \end{cases} \tag{8}$$

The derivation of the sensitivity of the objective function to the design variable is given in the Appendix. Finally, the overall normalized sensitivity of element i is defined as

$$\frac{\partial f}{\partial\rho} = \lambda_1\overline{\alpha}_m + \lambda_2\overline{\alpha}_l \tag{9}$$

where $\lambda_{1,2}$ $(\lambda_1 + \lambda_2 = 1, 0 \leqslant \lambda_{1,2} \leq 1)$ are weighting factors and $\overline{\alpha}_m = \frac{\partial f_m}{\partial\rho}\left(\max_i \frac{\partial f_{mi}}{\partial\rho}\right)^{-1}$ and $\overline{\alpha}_l = \frac{\partial f_l}{\partial\rho}\left(\max_i \frac{\partial f_{li}}{\partial\rho}\right)^{-1}$ represent the corresponding normalized sensitivities. Specifically, the normalized length constraint sensitivity $\overline{\alpha}_l$ should satisfy

$$\overline{\alpha}_l = \begin{cases} 1 - \frac{\partial f_l}{\partial\rho}\left(\max_i \frac{\partial f_{li}}{\partial\rho}\right)^{-1}, & \max_i \frac{\partial f_{li}}{\partial\rho} > 0 \\ 0, & \max_i \frac{\partial f_{li}}{\partial\rho} < 0 \end{cases} \tag{10}$$

In this study, the optimization formulation and procedure were implemented in MATLAB. The weight function λ_i depends on the particular coral species but is independent of the element sensitivity and thus could be determined before the finite element analysis. The design domain was discretized into $10^4 \sim 10^5$ (approximately 120×120, depending on the shape of the coral) four-node planar elements. Both the ridges and valleys were assumed to be homogeneous, and Neumann boundary conditions were applied to the external elements. The ratio of matter interchange between the ridges and valleys, σ, was set to 10^{-3}. In addition, a sensitivity filtering technique was applied as follows: $\frac{\partial\hat{f}}{\partial\rho} = \sum_{i\in\Omega_e} H_{ei}\rho_i\frac{\partial f}{\partial\rho}/\left(\rho_e\sum_{i\in\Omega_e} H_{ei}\right)$, where $H_{ei} = max(0, r_{min} - \Delta(e,i))$, with $\Delta(e,i)$ being the distance between elements e and i and r_{min}being the filter radius. Ω_e (the domain within the filter radius) was employed in the optimization procedure to avoid problems such as checkerboarding and mesh dependency. Notably, the filter radius was chosen to be $r_{min} = 2.0 \sim 5.0$, corresponding to the minimum dimensions of the wrinkles. The area fraction of valleys, $\chi = 0.2 \sim 0.6$, was determined based on the experimentally observed appearance of the reference corals. The upper area fraction ratio, $\gamma = 0.90 \sim 0.99$, was set to satisfy the length-scale control requirements. For the original polyps settled on the domain, their distribution was assumed to follow

$$\begin{cases} \mathbb{P}_{\Omega i} = p_0 \\ \overline{\rho_i(x_i,y_i)\rho_j(x_j,y_j)} \geqslant d_0, \rho_i, \rho_j \in \Omega \end{cases} \tag{11}$$

where $\mathbb{P}_{\Omega i}$ is the survival possibility of larva i in a specific part of the domain, Ωi. The possibility p_0 can vary in accordance with the nature of the species (some larvae prefer to congregate in specific locations, such as the center or edge of the domain.). $\rho_i = \rho_j = 1$ represents the first group of settled polyps, in which each pair is separated by a distance larger than d_0. This is because sufficient living space should be ensured for the polyp larvae, as polyps that are too close to each other will not survive.

Regular *Platygyra* structures can be obtained via the above optimization algorithm. The evolution history of the objective value and corresponding coral appearances are shown in Fig. 2. When the larvae have just settled in a limited space, the coral starts to grow in a disorderly manner around the first group of colonists. During this time, the normalized objective value sharply decreases during the early stage of evolution (from 100% to 40% during iterations 1–5). Afterward, the decrease in the objective value is retarded because the breeding of the polyps is accelerating, until the polyps occupy the entire domain (iterations 5–15). In iterations 15–22, the polyps are fighting for the last remaining space. They gradually evolve into winding shapes with a small number of bifurcations. The optimization process converges after 27 iterations, at which time a small number of closed loops appear in the polyps. These features cause water to circulate in the loops, resulting a slow flow rate and better efficiency of nutrient capture. The evolution of the optimization process indicates that the matter interchange characteristics of coral depend on the maze pattern of the polyps.

2.3. Shape, expansion and curvature

Most brain corals do not have perfectly rounded outlines. In contrast, due to space constraints (the shape of the base or the presence of other neighbors), they usually have irregular shapes. On the other hand, brain corals grow very slowly as each generation adds to the limestone skeleton. Benefiting from their massive, sturdy structures, brain corals form the foundation of coral reefs and can live nearly 1000 years. In other words, the slow growth process of brain corals might affect their groove patterns. To explore the influence of shape and the growth process on gully morphology, related programs were implemented in MATLAB, and the corresponding results were analyzed. In the early stage of an individual's growth process, fertilized larvae attach themselves to the seafloor or stones. The places where they settle determine the future living space of the coral. As seen in Fig. 3a and b, the early expansion is generally homogeneous, with the rough outline remaining essentially a convex polygon. The polyps prefer to grow along preformed contours, forming moat-like gullies.

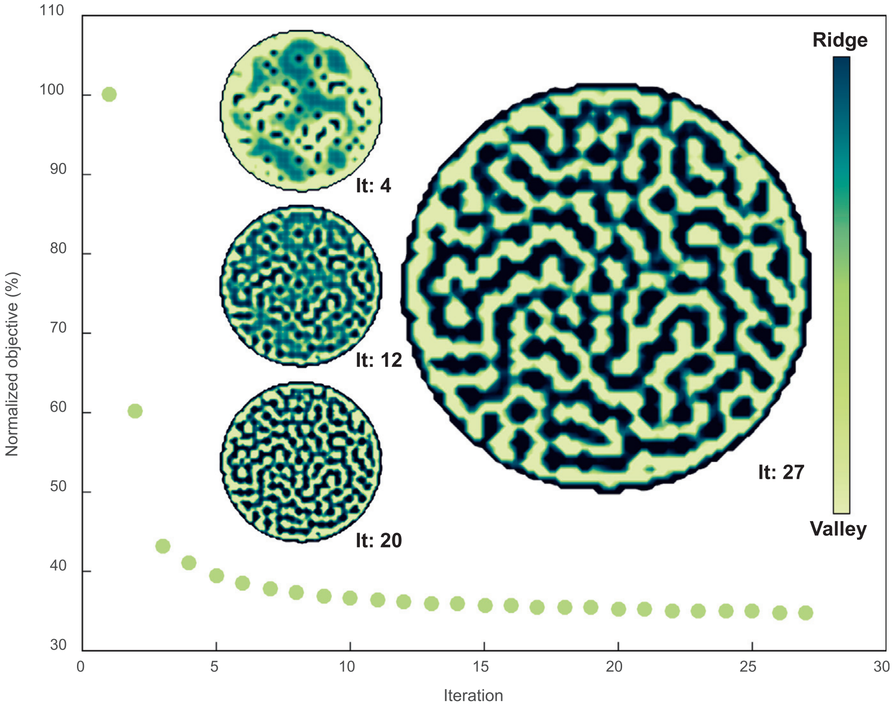

Fig. 2. Normalized objective value (%) versus the number of iterations of optimization. The corresponding evolution of *Platygyra* is also illustrated, where light colors represent valley regions and dark colors represent ridge regions. Iteration 4–Settling of the larvae. Iteration 12–Accelerated reproduction. Iteration 20–Bifurcation. Iteration 27–Stabilized layout.

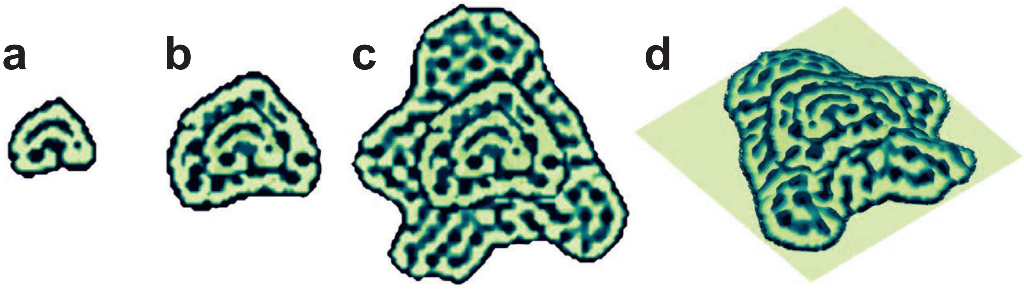

Fig. 3. Sketches of the evolution of an irregularly shaped *Platygyra* pattern: (a) the original state of the coral; (b) the state of the coral after homogeneous expansion; (c) the final appearance of the gully morphology with an anisotropic growth rate; (d) the corresponding dome-like 3D structure.

Notably, the shapes of the previously formed structures will not significantly change in the next phase of expansion. To ensure adherence to this rule in the evolutionary optimization process related to coral expansion, the design domain Ω_p was divided into several parts, one corresponding to each growth stage ($p = 2, 3, \ldots$). In each evolutionary step, the amplitude of the change in the density of each element was limited by ρ_{chmax}, defined as follows:

$$\rho_{chmax} = \begin{cases} \delta_p \rho_{ch}, & \rho \in \Omega_{p-1} \\ \rho_{ch}, & \rho \in \Omega_p \end{cases} \tag{12}$$

where the parameter $\rho_{ch} = 0.1$ determines the amplitude of the change in the density of each element between consecutive growth stages. As observed from mariculture, the further evolution of the region formed in the previous stage is quite slow. In quantitative terms, the change in the density was restricted by the parameter $\delta_p = 0.05$.

As the coral becomes stationary after the period of early expansion, the polyps will form buds at the bottom. Thus, expansion becomes much easier; however, surrounding obstacles such as stones or other colonies must be avoided. In this stage (Fig. 3c), a mature individual may grow in arbitrary directions depending on environmental conditions such as illumination, water flow and nutrients. Consequently, the directions of the gullies are no longer regular; they may sometimes even grow perpendicular to the previous contour or form closed loops.

Brain corals growing in high-flow environments exhibit higher growth rates than those growing in lower-speed currents because the water flow speeds up the transportation of nutrients. Therefore, the morphology of brain corals is elaborately formed to adapt to the current, especially to ensure stability under flowing water. Accordingly, a hemispherical shape is highly favorable. Limited by the available growth space, however, not all brain corals have perfectly spherical skeletons. In general, deeper water causes corals to have flatter structures, which could be better able to resist strong water pressure. According to the literature review and aquatic observations, most corals preferentially expand from the attachment surface and slightly swell vertically, forming a hill-like skeleton that can be mathematically represented as

$$\begin{cases} e & = min\left(\overline{AB}\right) \\ z_a & = 1 - \zeta(e - e_{max})^2 \end{cases} \tag{13}$$

where $A(x_a, y_a)$ is an element in the design domain Ω and $B(x_b, y_b)$ is an arbitrary element on its outline. The dome-like skeleton can be defined in terms of the 3D coordinates (x_a, y_a, z_a) along with a slope governing parameter ζ. In addition, a significant correlation between the surface roughness of coral and its matter interchange rate has been confirmed. In terms of biological species, corals with smooth surfaces have more space for larger individual polyps. Conversely, a wrinkled surface is able to increase nutrient capture from a fast water flow. On the other hand, corals with deep ridges have the ability to establish diverse environments with varying light and flow conditions, making them attractive to small creatures. Therefore, numerical simulation of the 3D morphology of the gullies is crucial. For this purpose, a formulation based on the local coordinate system can be written as follows:

$$A'\left(x'_a, y'_a, z'_a\right) = A(x_a, y_a, z_a) + g\rho_a \vec{m}_a \tag{14}$$

where $A'\left(x'_a, y'_a, z'_a\right)$ denotes the revised coordinates of the element $A(x_a, y_a, z_a)$. Corresponding to the aforementioned side-surface convention, the density at this location determines whether it belongs to a valley $(\rho_a \leqslant \rho_l)$ or a ridge $(\rho_a > \rho_l)$ in the design domain. The gully depth is proportional to the optimized density of a and is amplified by $g>0$ (the value of g is determined based on statistical data from aquatic observations), while the direction is determined by the external normal vector $\vec{m}_a$ on the surface. It is noted that the gully depth affects the optimization results through the efficiency of matter interchange. Finally, the 3D morphology corresponding to Fig. 3c is as shown in Fig. 3d.

2.4. Species and wrinkles

Generally, the wrinkle patterns of different brain coral species are diverse and correspond to their polyp growth characteristics. For instance, the various shapes formed by the polyps are strongly influenced by the water flow. Individuals in deep water exhibit lower calcification ratios, with wider gaps between neighboring polyps. In contrast, heavier calcification occurs in colonies living under rapid water flows, where dense cellular structures appear. Stony corals (*Scleractinia*) can also control the shapes of their colonies through budding and different relative growth rates in different locations. Buds can be classified into internal and external tentacle buds. In an internal tentacle bud, the polyps simply divide in the orifice; the bud retains part of the original orifice, while the remaining portion undergoes development. External tentacle buds appear outside the tentacle ring of the main body and cannot maintain the function of the main body. To reveal the principle of this interesting phenomenon, the evolution of coral wrinkle patterns was investigated. For *Platygyra* (Fig. 4a), the larvae have a relatively high survival rate according to the expression given in Eq. 11, with thin valley regions occupying nearly half of the area of the domain $(r_{min} = 3.0, p_0 = 80\%, d_0 = 3.0)$. On the other hand, the polyps of *Goniastrea* are arranged in a completely different way (Fig. 4b). The structure is usually composed of nubby skeletons, where the calices (0.003–0.005 m in the lateral dimension and 0.001–0.002 m in depth) are irregular polygons. Two neighboring calices are separated by the coenosteum, where a columella is connected to 12 septa and an equal number of phanic spindle-like paliform lobes. Another group of brain corals has a folded rather than spherical shape and lives in a free-standing manner rather than as part of the structure of a larger reef. These species are called open brain corals $(r_{min} = 3.0, p_0 = 5\%, d_0 = 1.0)$. *Lobophyllia*, as a genus of open brain corals commonly found in aquariums, is distinguished by tenacious vitality and a fluorescent protein that emits vibrant colors when exposed to blue light (Fig. 4c). Such corals usually exhibit a variety of brilliant fluorescent colors. They are composed of spiral-petal-like flaps that grow upward or inward at the edges. The reticular structure of the coenosteum of the polyps buckles into wrinkles. The wrinkled lobes are auricular or fan-shaped. Sometimes, however, other shapes also develop, such as

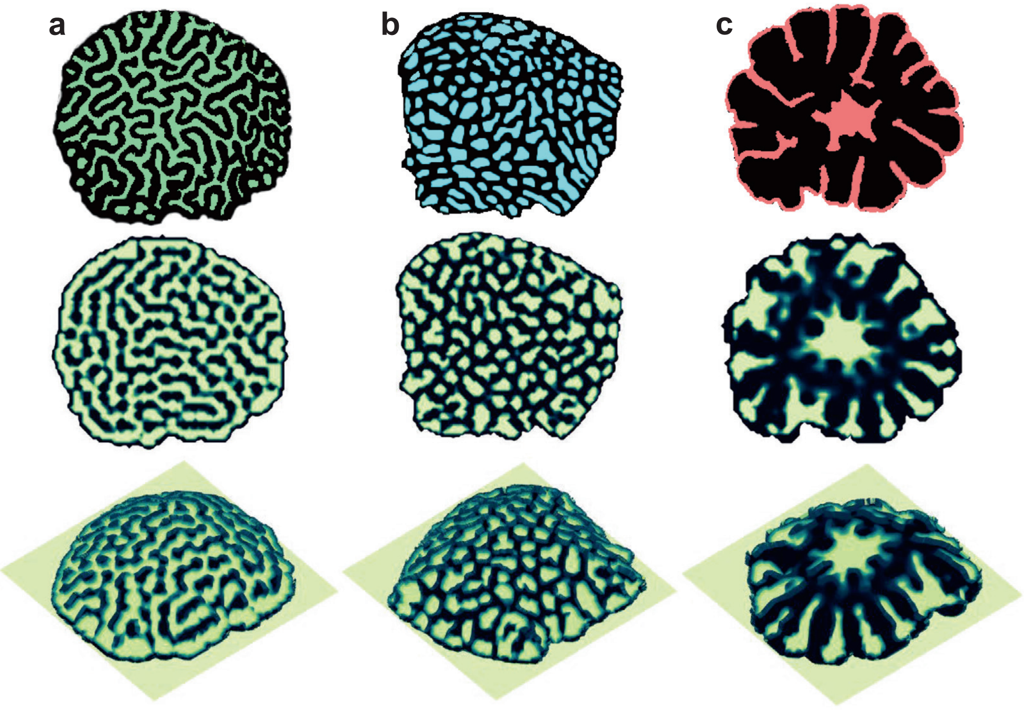

Fig. 4. The appearances of different brain coral species, represented by sketches of actual specimens (top row), simulated results (middle row) and 3D structures (bottom row): (a) *Platygyra*; (b) *Goniastrea*; (c) *Lobophyllia*.

more regular oval shapes or shapes with more protruding skeletons in the middle ($r_{min} = 5.0; p_0 = 70\%$ for the spiral-petal-like flaps and $p_0 = 2\%$ for the rest of the domain; $d_0 = 1.0$).

3. Numerical simulation

3.1. Vorticity analysis

Sufficient light allows *symbiotic algae* to grow normally and provide energy for the corals. A good flow environment provides not only plankton, which are carried by the water, but also protection to the corals, helping them to breathe and carrying away excreta and secretions. In such an environment, *Acropora* grows faster and appears denser, giving these corals an advantage in coral reefs because they can obtain more sunlight more easily. In addition, they can cut off the flow of water from other corals around them. Conversely, *Colpophyllia* does not exhibit aggressivity due to having no sharp edges, yet these corals can still gain competitive superiority. When a neighbor is within striking range, the sweeper tentacles of brain corals can stretch 10 times in length to attack the invader with the current. In addition, *Colpophyllia*, like *Platygyra sinensis*, not only extends its tentacles on the side facing the invading corals but also randomly radiates a small number of tentacles in different directions for detection. Similar sweeper tentacles have been found in many genera, including *Goniastrea*, *Acanthastrea*, *Favia*, *Favites* and *Galaxea*.

The fluid dynamics, especially the turbulence, around brain corals is a crucial basis for studying the matter interchange efficiency of artificial corals. The seawater movement considered in this research can be regarded as the horizontal sloshing of a homogeneous, isotropic and viscous Newtonian fluid described in a fixed Cartesian coordinate system with reference to an oscillating rectangular chamber. In the numerical model, the spatial and temporal discretization scheme of the lattice Boltzmann method (LBM) [38] was adopted. For the Smagorinsky eddy viscosity, the filtered particle distribution function $\bar{f}_v(\mathbf{n}, t)$ was employed, where the cap represents a filtering operator, $\mathbf{n}$ denotes the coordinate tensor of the particles, t is the time variable and v represents a velocity orientation. The iterative temporal process followed the forced Bhatnagar–Gross–Krook (BGK) model [39], consisting of a collision step and a streaming step, as follows:

$$\tilde{\bar{f}}_v(\mathbf{n}, t) = \bar{f}_v(\mathbf{n}, t) - \frac{\Delta t}{\kappa^*}\left[\bar{f}_v(\mathbf{n}, t) - \bar{f}_v^{eq}(\mathbf{n}, t)\right] + \bar{F}_v \Delta t \tag{15}$$

$$\bar{f}_v(\mathbf{n} + \mathbf{D}_v \Delta t, t + \Delta t) = \tilde{\bar{f}}_v(\mathbf{n}, t) \tag{16}$$

where $\tilde{\bar{f}}_v$ is the postcollision distribution function, $\mathbf{D}_v$ is the fluid speed tensor, and κ^* is the relaxation time corresponding to the total viscosity v^*. The external force $\bar{\mathbf{F}}_v$ is fixed on the oscillating chamber from the noninertial reference frame. The formula for the equilibrium distribution function $\bar{f}_v^{eq}$ is as follows:

$$\bar{f}_v^{eq}(\mathbf{n}, t) = \omega_v \rho_f \left[1 + \frac{\mathbf{u}_f \cdot \mathbf{c}_v}{c_s^2} + \frac{(\mathbf{u}_f \cdot \mathbf{c}_v)^2}{2c_s^4} - \frac{\mathbf{u}_f \cdot \mathbf{u}_f}{2c_s^2}\right] \tag{17}$$

where c_s is the speed of sound propagation in the lattice and ρ_f and $\mathbf{u}_f$ are the macroscopic density and velocity, respectively, of the fluid, which can be calculated from the distribution function as follows:

$$\rho_f = \sum_{v=0}^{18} \bar{f}_v, \mathbf{u}_f = \frac{1}{\rho_f} \sum_{v=0}^{18} \bar{f}_v \mathbf{c}_v + \frac{\bar{\mathbf{F}} \Delta t}{2} \tag{18}$$

According to a related study [40], the force term $\bar{F}_v$ can be expressed as

$$\bar{F}_v = \omega_v \left(1 - \frac{1}{2\kappa}\right) \left[\frac{\mathbf{c}_v - \mathbf{u}_f}{c_s^2} + \frac{\mathbf{c}_v(\mathbf{c}_v \cdot \mathbf{u}_f)}{c_s^4}\right] \cdot \bar{\mathbf{F}} \tag{19}$$

Here, ω_v is a weighting factor related to the lattice velocity, which can be derived from the D3Q19 model [38].

Numerical CFD simulations were conducted in a domain of $1.0\text{m} \times 0.3\text{m} \times 0.3\text{m}$. For both the upper and lower boundaries, slip boundary conditions were employed, while periodic boundary conditions were adopted on both lateral sides. At the inlet, a uniform velocity of 0.1 m/s was employed, and free outlet boundary conditions were used. Additionally, octree element structures with a minimum mesh size of 0.001 m were used for local encryption surrounding the coral structure. A convergence test was performed to verify the mesh independence.

In Fig. 5, the periodic changes in the surface and the surrounding vorticity of artificial coral under unidirectional turbulence are represented in sequence, and some characteristics of the flow field affecting matter exchange are noted. Generally, the variation in vorticity is entirely caused by periodic vortex shedding. The maximum vorticity occurs at the ridges on the side facing the current, causing a relatively smooth laminar flow to envelop the back side of the coral. Under these circumstances, the polyps in the valleys are well shielded from the dangers presented by the current, including sharp objects and fierce predators. On the other hand, flow reversal occurs on the back side of the coral when vortex shedding begins. The periodic change in the flow line spectrum could cause a change in the pressure distribution, which would lead to a change in the magnitude and direction of the fluid pressure acting on the coral and ultimately cause vibration of the coral.

To analyze the influence of the morphological characteristics of brain coral on the surrounding seawater flow field, models were generated using various combinations of the slope (ζ) and fold depth (g) parameters. Through CFD simulations, vorticity distributions similar to those in Fig. 5 were obtained, and the corresponding results are shown in Table 1. For a better quantitative analysis of the water flow, the mean vorticity in the space close to the coral surface (0–3 cm) was computed for comparison. The results show that when the slope is small $\zeta \leqslant 0.0001$ (corresponding to a flat shape), rapid vortices cannot be generated on the side facing the current. Such vortices could increase the amount of time nutrients would remain in contact with the polyps, which would increase the efficiency of matter interchange. As a result, most brain corals form hemispherical structures. However, a large ζ leads to a great impact from the seawater that is detrimental to the coral's stability. Therefore, the value of ζ usually should not exceed 0.0003. On the other hand, as the most distinct morphological characteristics of brain corals, the grooves can collect microorganisms that fall from vortices, providing the polyps with nutrients other than those obtained through photosynthesis. Rougher surface features ($g \geqslant 2.00$) create strong vortices that allow polyps to capture abundant food through their tentacles. However, this also results in low efficiency for seawater to carry the polyps' fertilized eggs and excreted metabolites. Over time, such matter will be deposited in the gullies, preventing the population from reproducing. In conclusion, vorticity analysis can be applied to more reasonably determine the values of 3D morphological parameters for coral evolution. The flow chart of the whole optimization process is shown in Fig. 6.

At the moment representing the worst conditions, for a hemispherical structure with a fixed bottom, a maximum stress of 2.71×10^2 Pa occurs on the side facing the current (Fig. 5(c)). This is a safe value for solid structures predominantly consisting of calcium carbonate (which has a strength limit of approximately 1×10^6–2×10^6 Pa). Moreover, a relatively large stress is also found at the pole facing away from the current, which is a result of the

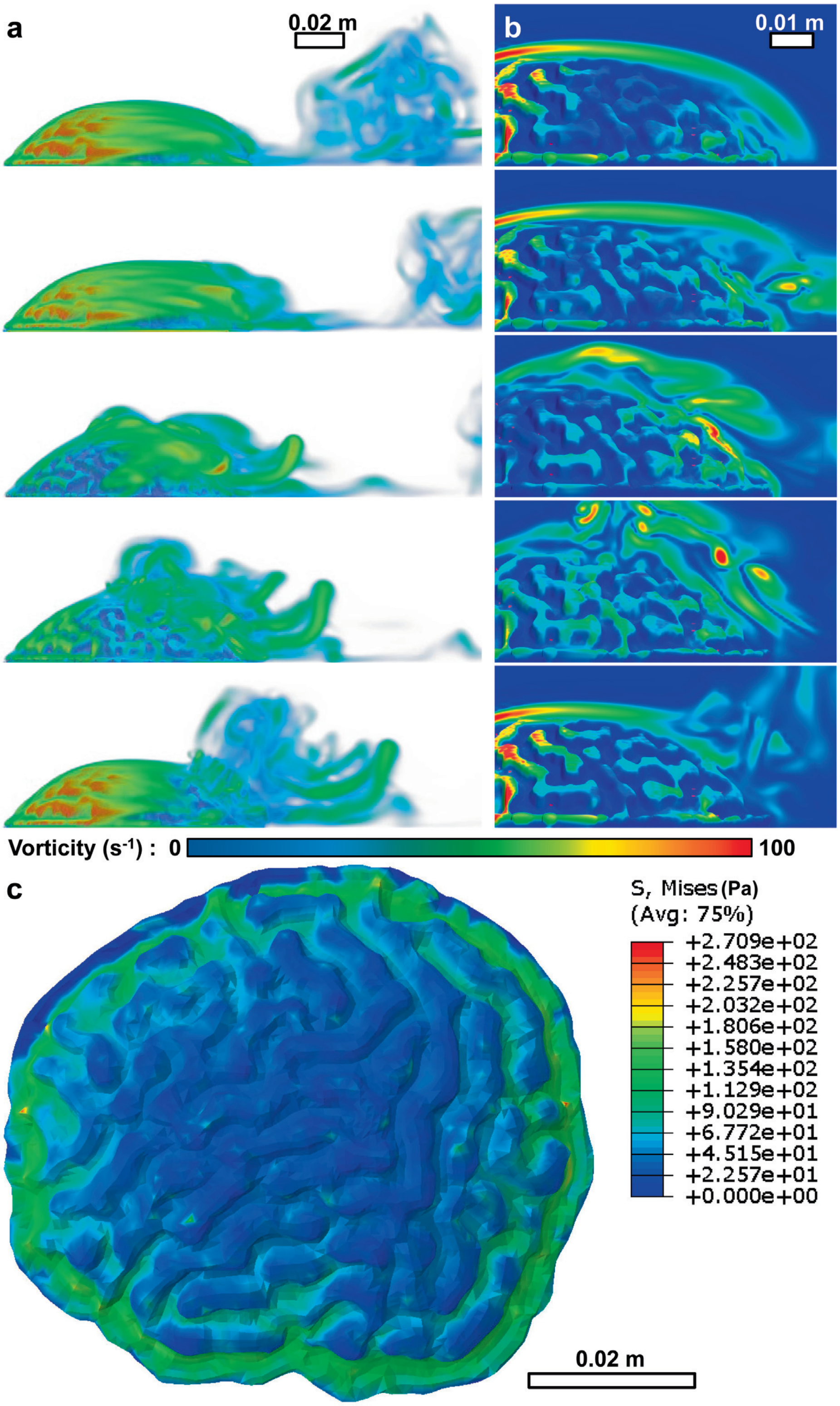

Fig. 5. The vorticity and surface-stress contours of artificial brain coral: (a) one wave cycle from the global perspective; (b) the corresponding local perspective on the reverse side of the coral; (c) the corresponding stress contours under the worst-case conditions.

flow reversal. In fact, the stress resulting from hydrostatic pressure is often much greater than the stress caused by ocean currents. Due to its bulbous shape, *Platygyra* has less to fear from pressure and currents than staghorn coral and thus tends to live on deeper seabeds (approximately 30–50 m).

3.2. Matter interchange simulation

To study the influence of the gully structure of brain coral on matter exchange, the Fluent module of the commercial finite element software ANSYS (ANSYS, Inc., United States) was employed

Table 1
Summary of the influence of the morphological characteristics of brain coral on the surrounding vorticity.

Case	ζ	g (mm)	Mean vorticity near the surface (s^{-1})
1	0.0001	1.50	15.72
2	0.0001	2.00	18.68
3	0.0001	2.50	21.49
4	0.0002	1.50	17.16
5	0.0002	2.00	21.52
6	0.0002	2.50	24.33
7	0.0003	1.50	19.41
8	0.0003	2.00	23.27
9	0.0003	2.50	26.55

to simulate the matter interchange process in a static water environment. The numerical model was imported into the software and placed in a chamber filled with solving liquid. The pressure-based solver was employed, using the transient solution process and a given gravitational field. Regarding the material-related assumptions, the liquid domain and the valleys of the brain coral were set as liquid (water) materials, whereas it was assumed that the ridges could not be dissolved. For the boundary conditions, the concentration of the liquid against the chamber was set to 0. Both the solid and liquid domains were discretized into tetrahedral elements, with the coral and liquid containing 78938 and 161765 elements, respectively. The process could be interpreted as the valleys of the brain coral gradually being dissolved into the surrounding liquid until they were completely dissolved. The simulation was conducted using the SIMPLE algorithm, and the results are presented in the figure below.

The dissolution process began in the upper right region of the man-made coral; this relative location was subject to some randomness (Fig. 7a). However, the matter-interchange-sensitive region (valleys) occupied a relatively large area proportion in the upper right corner, which was one of the reasons for the active matter interchange here. From another point of view, dissolution generally occurred at the edges of the valleys. This be explained by the fact that the dissolution process started at random spots, from which it then spread. However, at the junctions of valleys and ridges, the surface curvature of the model varies greatly over a short distance. For dissolution spots at these junctions, the solution containing the dissolved matter tended to be trapped, making it difficult to enter outside circulation. Consequently, the dissolution along the valley edges was accelerated (Fig. 7b&c). Then, the centers of the valleys also started to dissolve (Fig. 7d&e), and the dissolution process gradually spread to the entire dissoluble domain (Fig. 7f).

4. Experimental justification

4.1. Mold prefabrication

Because of the complex geometry and slump of coral structures, it would be difficult to use direct printing techniques such as fused deposition modeling (FDM) for fabrication. Therefore, a soft material with good demolding performance was used for the manufacture of casting molds. First, we imported the optimized structure into the commercial 3D modeling application ZBrush (version 2020, Pixologic Inc.) (Fig. 8a). Then, the numerical coral model

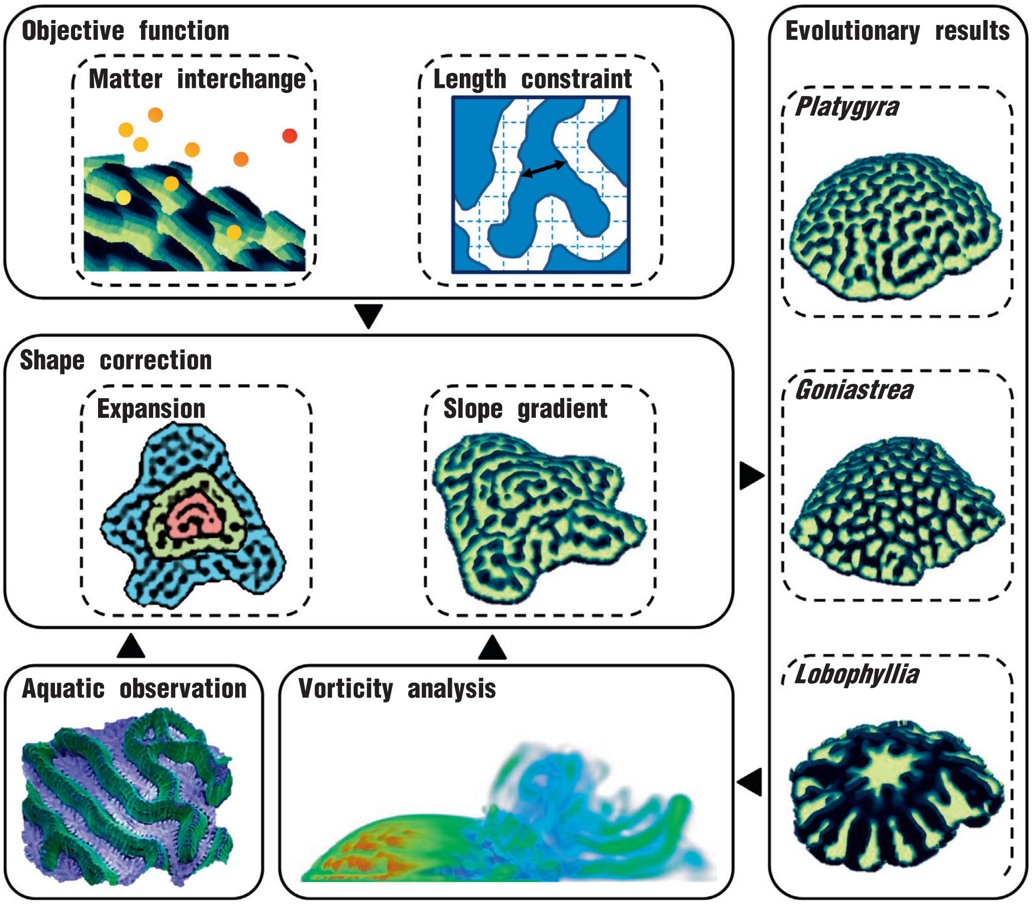

Fig. 6. Flow chart showing the step-by-step process of evolutionary optimization.

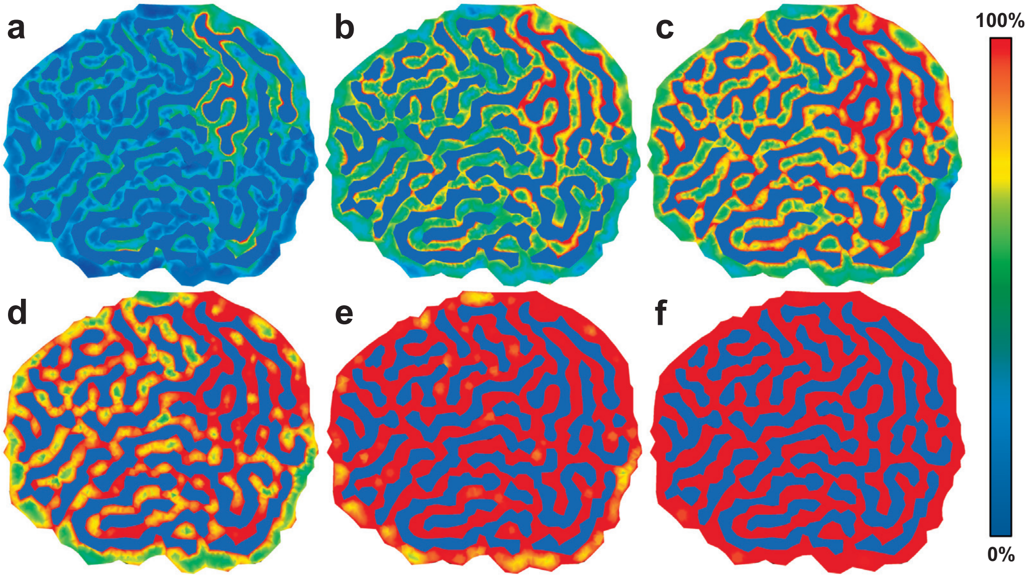

Fig. 7. Simulation of the matter interchange process for *Platygyra*: (a) a state in which 15.24% of the polyps (cyan parts) have completed matter interchange; (b-f) similarly, states of (b) 35.63%, (c) 47.24%, (d) 60.51%, (e) 79.77%, and (f) 100% completion. The color bar represents the percentage of polyps that have completed matter interchange.

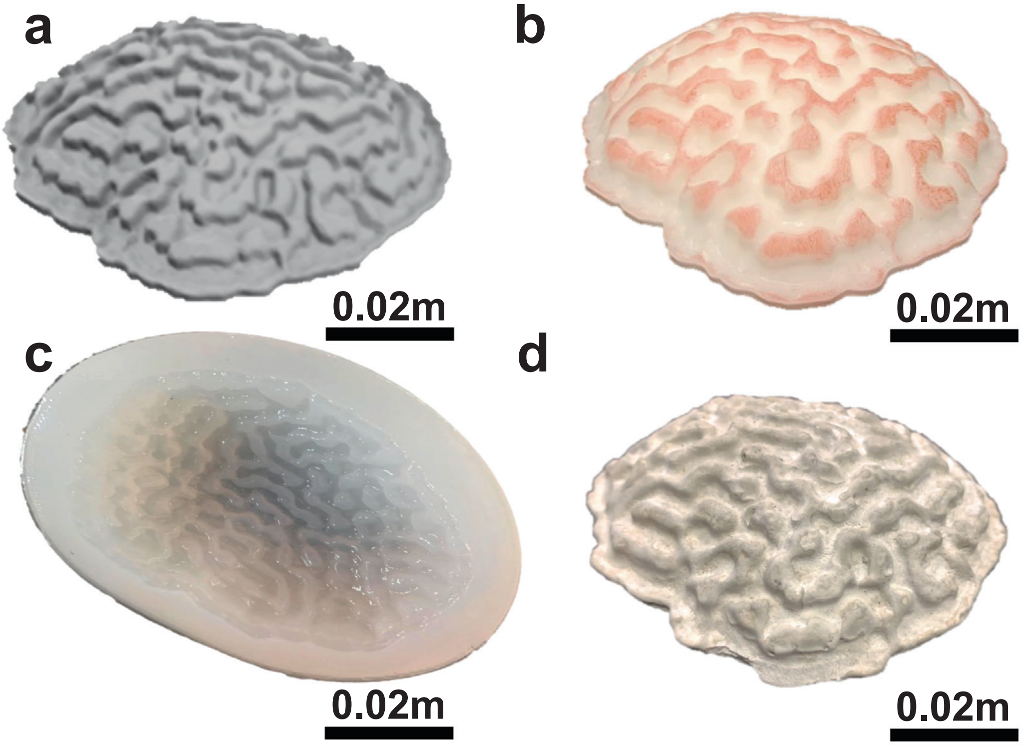

Fig. 8. The fabrication procedure for man-made *Platygyra*: (a) the polished geometric model; (b) the UV-curable resin model fabricated using the DLP technique; (c) the reverse mold made of platinum AB silica gel; (d) the cast *Platygyra* model made of a cement and calcium carbonate mixture.

was printed using UV-curable resin (SP-RH; Soonsolid Co., Ltd., China; density: 1.14 $\times 10^3$kg/m^3; curing wavelength: 4.05 $\times 10^{-7}$ m; viscosity (25 °C): 1.06 $\times 10^8$ Pa·s) by a desktop digital light processing (DLP) printer (SprintRay Pro; Soonsolid Co., Ltd., China) (Fig. 8b). We used this printing method because of its high printing resolution, which could help to maintain the geometrical configuration of the numerical model. The printer had a 10^{-4} m printing precision, a 6×10^{-5} m layer thickness, and a printing time of 10 s per layer. It took approximately 30 min to fabricate a 0.0708 m × 0.0644 m × 0.0190 m sample. Afterward, a reverse mold was fabricated using platinum AB silica gel (SJ3212 Beijing Sanjing Xinde Technology Co., Ltd., China; Shore A hardness: 15) (Fig. 8c). After the mold had solidified, artificial corals were fabricated via a casting process (Fig. 8d).

4.2. Casting process

The specimens were composed of a material that provided strength (Portland cement PO42.5) and a material that satisfied the necessary requirements in terms of biological properties (calcium carbonate powder, fineness 800). To study the strength of the artificial coral composites, the proportions of these two solid matter materials were employed as the influencing factors for orthogonal experiments. The various environmentally friendly compositions employed for manufacturing [41], all of which are similar to the composition of stony corals, are shown in Table 2. To prepare the cementitious composites, the two powders were first poured into a mixer for dry mixing. Afterward, the mixed concrete was poured into the mold, and the top surface was leveled. The mold was removed after three days of curing at a temperature of 20.0 ± 2°C and a relative humidity of 95 ± 5%. Then, the sample was covered with plastic film and further cured for 25 days. Additionally, to compare the strengths of the various recipes, we prepared corresponding standard cubic blocks (0.15 m × 0.15 m × 0.15 m) with the same mixture proportions. For compression tests, a compression testing machine (CONCRETO 2000; Shimadzu Co., Ltd., Japan) was employed, whose loading speed was controlled at 0.3 MPa/s. Each group of samples was subjected to compression three times, and the average results were recorded. Generally, the compressive strength decreased as the proportion of calcium carbonate in the composites increased. According to the CFD simulations, the compressive strength of the S4 material was still more than sufficient to withstand the current impact and hydrostatic pressure at a depth of 50 m. Furthermore, such a mixture with high calcium carbonate content is closer to the composition of natural coral than plain cement is. However, a high calcium carbonate content will also lead to a decrease in workability, especially in terms of the cohesion of the concrete. In summary, the mixture proportions of the S4 material were found to be the most suitable for the manufacture of this man-made coral.

Table 2
Mixture proportions and compressive strength of the materials used for the fabrication of man-made corals

Sample label	Cement (g)	Calcium carbonate (g)	Water (g)	Compressive strength (MPa)
S1	33.3	33.3	33.3	11.390 ± 0.826
S2	30.3	36.3	33.3	7.197 ± 0.534
S3	27.8	38.8	33.3	5.537 ± 0.311
S4	25.6	41.0	33.3	4.384 ± 0.285

4.3. Matter interchange test

To verify the superiority of the optimized brain-shaped grooves in terms of their matter interchange capabilities, a pair of control samples were fabricated for calcium carbonate–acetic acid corrosion experiments. The test process was performed as follows: First, a sample with concentric ring-shaped gullies was cast, whose ridges and valleys each occupied half the surface area (Fig. 9a).

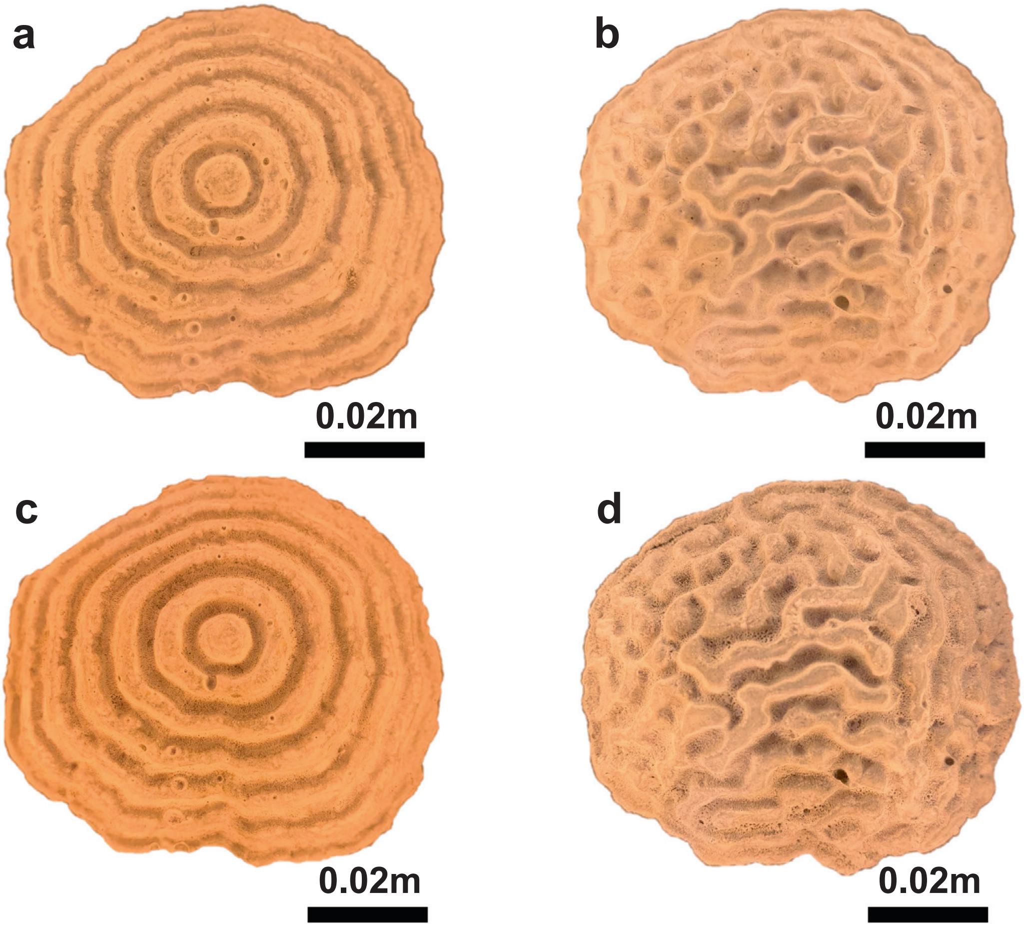

Fig. 9. Control experiment to validate the matter interchange capability: (a) the original man-made coral with concentric ring-shaped gullies; (b) the original man-made *Platygyra*; (c) the coral with concentric ring-shaped gullies after the matter interchange test; (d) the man-made *Platygyra* after the matter interchange test.

For comparison, a man-made *Platygyra* sample was cast using the topological optimization method described above, where the valleys also occupied 50% of the sample area (Fig. 9b). The samples were photographed with a digital camera (12 million pixels) (Fig. 9b) were each subsequently placed at the bottom of a chamber of the same size as the seawater tank for coral cultivation (0.80 m × 0.50 m × 0.80 m), with a propeller pump placed 0.4 m away from the sample. Because the predation behavior of the polyps occurs within the valleys, the observations needed to focus on the valleys rather than the ridges. It was therefore necessary to preprocess the models by pasting plastic film on all ridge surfaces in Fig. 9a,b. In this way, it was ensured that the matter interchange reaction would occur only in the valleys, as these were the only parts of the samples that were in contact with the solution. After the chamber was filled with pure water, the flow speed was controlled by the pump at 2000 gph. Every 60 s, 10 ml of 80% acetic acid solution was dropped into the chamber from a burette beside the pump. One hour later, the sample was removed, and its surface was rinsed with deionized water before drying. According to the observation of the concentric ringed structure after corrosion (Fig. 9c), the calcium carbonate in the structure reacted with the acetic acid to form calcium acetate, which then dissolved in the water, leaving a few tiny holes in the valleys. These holes were fairly evenly distributed throughout all of the gullies. In contrast, the valleys of the man-made *Platygyra* exhibited many holes of different sizes (Fig. 9d). Generally, the matter interchange reaction was more severe on the man-made *Platygyra*, especially in the valleys at an intermediate height from the bottom. This difference can be explained by the flow field simulation. Normally, the grooves tend to block water from flowing over the ridges and force it to run along the valleys. Thus, circular water flows form in the concentric grooves. The flow carrying the acetate ions reacts with the calcium carbonate, and the products of this reaction gradually precipitate from the valley surfaces and accumulate. This prevents the remaining calcium carbonate from coming in contact with acetic acid, resulting in insufficient material interchange. In contrast, after entering the man-made *Platygyra*, the water flow travels through the crisscross valleys and finally escapes from the gullies, carrying away the calcium acetate produced by the reaction. This allows the subsequent replacement reaction to continue, resulting in more extensive material interchange between the coral surface and the water. In other words, the brain-like surface maintains the concentration of nutrients while hindering the deposition of harmful substances.

To observe the micromorphology on the surfaces after the matter interchange treatment, the samples were rinsed and observed using a digital microscope capable of showing details as small as 4×10^{-7} m (DVM6, Leica, Germany). As seen from the optical images, the valley surfaces of both the coral with the concentric ring-shaped gullies (Fig. 9d) and the man-made *Platygyra* (Fig. 10b) were flat and nonporous. However, after the corrosion treatment, the microstructures of the two models were completely different. Calcium acetate was deposited on the surface of the concentrically ringed sample and prevented further corrosion. Under these conditions, only a small proportion of the calcium carbonate particles could react with acetic acid to produce carbon dioxide. Pores of approximately 10–70 microns in diameter were observed on the surface of the sample, with an average spacing of approximately 100 microns (Fig. 10c). On the other hand, matter interchange in the valleys of the man-made *Platygyra* was unhindered. A large number of pores with a spacing of approximately 80 microns are visible in Fig. 10d.

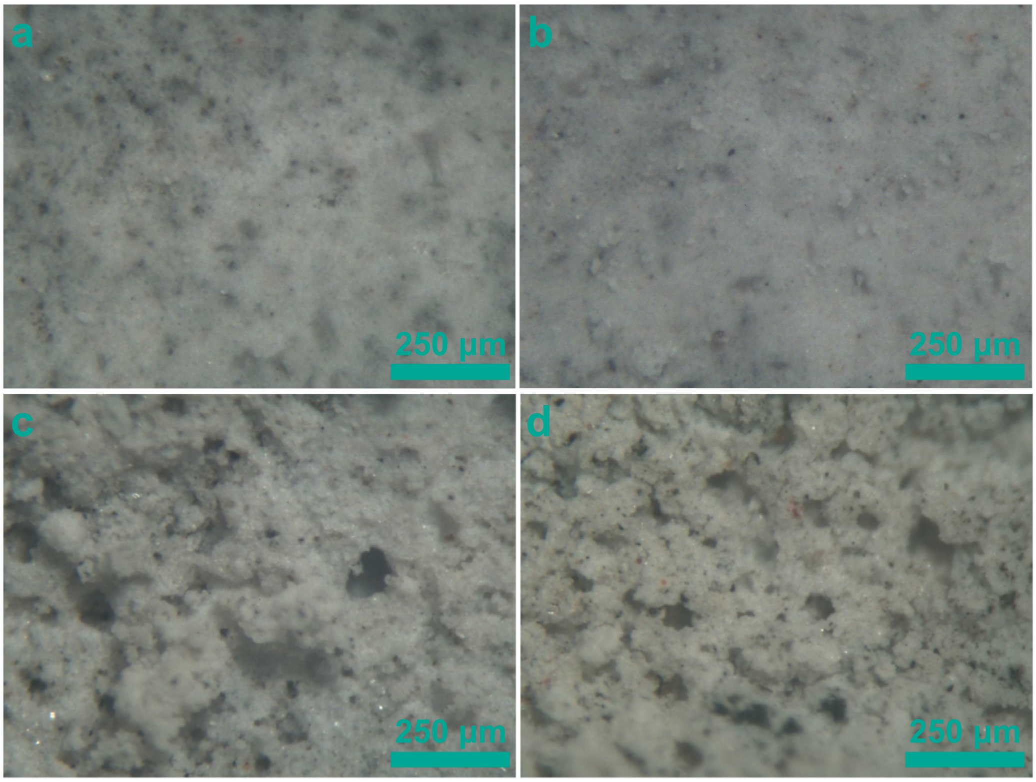

Fig. 10. The micromorphology on the valley surfaces of (a) the original man-made coral with concentric ring-shaped gullies; (b) the original man-made *Platygyra*; (c) the coral with concentric ring-shaped gullies after the matter interchange test; (d) the man-made *Platygyra* after the matter interchange test.

5. Conclusion

For the topological optimization of artificial coral structures, their resistance to matter interchange was minimized in the projected surface domain under length constraints. This optimization algorithm was proven to be correct by comparison with the morphological characteristics and growth processes of *Platygyra*, *Goniastrea* and *Lobophyllia*. In addition, CFD simulations showed that these artificial corals could provide shelter to shield polyps from swift currents and predators. A reverse mold was prepared from silica gel and used to cast models from mixtures of cement and calcium carbonate, where the mixture ratio was determined based on tests of compressive strength and biological adaptation. Finally, a numerical simulation and an acid corrosion test were conducted to verify the matter interchange capability of the optimized morphology with many folds.

The numerical and experimental validations showed that the brain-like folds contribute to the circulation of seawater, thus maintaining the concentration of nutrients and hindering the deposition of harmful substances. Multiobjective optimization based on a linear weighted sum can address some of the challenges of biological evolution mechanisms, especially those that are difficult to express mathematically. The presented optimization methodology is able to generate 3D topologies with promising matter interchange performance. Additionally, based on data from aquatic observations, the morphological characteristics of different species of brain corals could be successfully numerically reproduced by suitably arranging the settlement of the larvae.

However, only the matter interchange capability was considered in this study to evaluate the performance of the optimized structures. In fact, the biological process of coral growth is lengthy and influenced by a combination of factors, such as temperature and light intensity, for which accurate mathematical descriptions are still lacking. Strongly universal methods such as evolutionary optimization algorithms might be applied to analyze these problems. In subsequent work, the colonization and reproduction of polyps on artificial coral surfaces will be investigated. Regarding industrial applications, the results of this study might assist in the design of structures that can adsorb hazardous substances, particularly in oscillatory flows, which could help to effectively improve water and air quality in various environments.

Declaration of Competing Interest

The authors declare that they have no known competing financial interests or personal relationships that could have appeared to influence the work reported in this paper.

Acknowledgments

The authors gratefully acknowledge financial support from the National Natural Science Foundation of China (No. 11802082, 51908201), the Natural Science Foundation of Hunan Province (No. 2020JJ5027, 2020JJ5024), and the State Key Laboratory of Advanced Design and Manufacturing for Vehicle Body (51965009).

Appendix A. Sensitivity analysis

With the goal of solving the governing equation of f_m, the elemental-based matter transport matrix $\mathbb{K}$ is given by

$$\mathbb{K} = k(\rho)\mathbf{B}^T\mathbf{B} \tag{A.1}$$

where $\mathbf{B}$ determines the relation between the growing matter content and its spatial derivative. Accordingly, the discretized Lagrangian function can be rewritten as

$$\mathbb{L} = \mathbf{T}^T\mathbb{K}\mathbf{T} + \mathbb{T}^T(\mathbf{KT} - \mathbb{F}) \tag{A.2}$$

where $\mathbf{KT} = \mathbf{C}$ and $\mathbb{F}$ is independent of the design. The sensitivity of the density can be expressed as

$$\frac{\partial f_m}{\partial \rho} = \frac{\partial \mathbb{S}}{\partial \rho}\left(\mathbf{T}^T\frac{\partial \mathbb{K}}{\partial \mathbb{S}} + \mathbb{T}^T\frac{\partial \mathbf{K}}{\partial \mathbb{S}}\right)\mathbf{T} \tag{A.3}$$

where $\mathbb{S} = \sigma + (1-\sigma)\rho^p$. The adjoint problem of solving $\mathbb{T}$ can be expressed as

$$\mathbf{K}^T\mathbb{T} = -\left(\mathbb{K} + \mathbb{K}^T\right)\mathbf{T} \tag{A.4}$$

Both $\mathbf{K}$ and $\mathbb{K}$ are symmetric. Therefore, the adjoint problem can be solved through back substitution.

References

[1] Tagliafico A, Rangel S, Kelaher B, Scheffers S, Christidis L. A new technique to increase polyp production in stony coral aquaculture using waste fragments without polyps. Aquaculture 2018;484:303–8. https://doi.org/10.1016/j.aquaculture.2017.09.021.

[2] Musco L, Prada F, D'nna G, Galasso NM, Pipitone C, Vega Fernández T, et al. Turning casualty into opportunity: fragmenting dislodged colonies is effective for restoring reefs of a mediterranean endemic coral. Ecol Eng 2017;98:206–12. https://doi.org/10.1016/j.ecoleng.2016.10.075.

[3] Abaya LM, Wiegner TN, Beets JP, Colbert SL, Carlson KM, Kramer KL. Spatial distribution of sewage pollution on a hawaiian coral reef. Mar Pollut Bull 2018;130:335–47. https://doi.org/10.1016/j.marpolbul.2018.03.028.

[4] Giusti M, Canese S, Fourt M, Bo M, Innocenti C, Goujard A, et al. Coral forests and derelict fishing gears in submarine canyon systems of the ligurian sea. Prog Oceanogr 2019;178:102186. https://doi.org/10.1016/j.pocean.2019.102186.

[5] Bradley P, Jessup B, Pittman SJ, Jeffrey CF, Ault JS, Carrubba L, et al. Development of a reef fish biological condition gradient model with quantitative decision rules for the protection and restoration of coral reef ecosystems. Mar Pollut Bull 2020;159:111387. https://doi.org/10.1016/j.marpolbul.2020.111387.

[6] Tan F, Yang H, Xu X, Fang Z, Xu H, Shi Q, et al. Microplastic pollution around remote uninhabited coral reefs of nansha islands, south china sea. Sci Total Environ 2020;725:138383. https://doi.org/10.1016/j.scitotenv.2020.138383.

[7] Yu H, Da B, Ma H, Dou X, Wu Z. Service life prediction of coral aggregate concrete structure under island reef environment. Constr Build Mater 2020;246:118390. https://doi.org/10.1016/j.conbuildmat.2020.118390.

[8] Jiang Z, Liang Z, Zhu L, Guo Z, Tang Y. Effect of hole diameter of rotary-shaped artificial reef on flow field. Ocean Eng 2020;197:106917. https://doi.org/10.1016/j.oceaneng.2020.106917.

[9] Todinanahary GGB, Lavitra T, Andrifanilo HH, Puccini N, Grosjean P, Eeckhaut I. Community-based coral aquaculture in madagascar: A profitable economic system for a simple rearing technique? Aquaculture 2017;467:225–34. https://doi.org/10.1016/j.aquaculture.2016.07.012.

[10] Ramesh C, Koushik S, Shunmugaraj T, Murthy M. Seasonal studies on in situ coral transplantation in the gulf of mannar marine biosphere reserve, southeast coast of tamil nadu, india. Ecol Eng 2020;152:105884. https://doi.org/10.1016/j.ecoleng.2020.105884.

[11] Xia L, Lin S, Ma G. Stress-based tool-path planning methodology for fused filament fabrication. Additive Manuf 2020;32:101020. https://doi.org/10.1016/j.addma.2019.101020.

[12] Ruhl EJ, Dixson DL. 3d printed objects do not impact the behavior of a coral-associated damselfish or survival of a settling stony coral. PLoS ONE 2019;14:e0221157. https://doi.org/10.1371/journal.pone.0221157.

[13] Hesterberg SG, Duckett CC, Salewski EA, Bell SS. Three-dimensional interstitial space mediates predator foraging success in different spatial arrangements. Ecology 2017;98. https://doi.org/10.1002/ecy.1762.

[14] Hylkema A, Debrot AO, Osinga R, Bron PS, Heesink DB, Izioka AK, et al. Fish assemblages of three common artificial reef designs during early colonization. Ecol Eng 2020;157:105994. https://doi.org/10.1016/j.ecoleng.2020.105994.

[15] Lai Y, Li Y, Cao H, Long J, Wang X, Li L, et al. Osteogenic magnesium incorporated into plga/tcp porous scaffold by 3d printing for repairing challenging bone defect. Biomaterials 2019;197:207–19. https://doi.org/10.1016/j.biomaterials.2019.01.013.

[16] Becker A, Taylor MD, Folpp H, Lowry MB. Managing the development of artificial reef systems: The need for quantitative goals. Fish Fish 2017. https://doi.org/10.1111/faf.12288.

[17] Polak O, Shashar N. Can a small artificial reef reduce diving pressure from a natural coral reef? lessons learned from eilat, red sea. Ocean Coastal Manage 2012;55:94–100. https://doi.org/10.1016/j.ocecoaman.2011.10.006.

[18] Bertucci A, Moya A, Tambutté S, Allemand D, Supuran CT, Zoccola D. Carbonic anhydrases in anthozoan corals- a review. Bioorganic Medicinal Chem 2013;21:1437–50. https://doi.org/10.1016/j.bmc.2012.10.024, carbonic Anhydrase.

[19] Singh T, Kumar S, Sehgal S. 3d printing of engineering materials: A state of the art review. Mater Today: Proc 2020;28:1927–31. https://doi.org/10.1016/j.matpr.2020.05.334.

[20] Li L, Xiao B, Fang Z, Xiong Z, Chu S, Kwan A. Feasibility of glass/basalt fiber reinforced seawater coral sand mortar for 3d printing. Additive Manuf 2021;37:101684. https://doi.org/10.1016/j.addma.2020.101684.

[21] Lin S, Chen L, Zhang M, Xie Y, Huang X, Zhou S. On the interaction of biological and mechanical factors in leaf vein formation. Adv Eng Softw 2020;149:102905. https://doi.org/10.1016/j.advengsoft.2020.102905.

[22] Lin S, Xie YM, Li Q, Huang X, Zhang Z, Ma G, et al. Shell buckling: from morphogenesis of soft matters to prospective applications. Bioinspirat Biomimet 2018;13:051001. https://doi.org/10.1088/1748-3190/aacdd1.

[23] Ghasemi H, Park HS, Rabczuk T. A multi-material level set-based topology optimization of flexoelectric composites. Comput Methods Appl Mech Eng 2018;332:47–62. https://doi.org/10.1016/j.cma.2017.12.005.

[24] Anitescu C, Atroshchenko E, Alajlan N, Rabczuk T. Artificial neural network methods for the solution of second order boundary value problems. Comput Mater Continua 2019;59:345–59. https://doi.org/10.32604/cmc.2019.06641.

[25] Samaniego E, Anitescu C, Goswami S, Nguyen-Thanh V, Guo H, Hamdia K, et al. An energy approach to the solution of partial differential equations in computational mechanics via machine learning: Concepts, implementation and applications. Comput Methods Appl Mech Eng 2020;362:112790. https://doi.org/10.1016/j.cma.2019.112790.

[26] Li B, Hong J, Yan S, Liu H, Ge L. Generating optimal heat conduction paths based on bionic growth simulation. Int Commun Heat Mass Transfer 2017;83:55–63. https://doi.org/10.1016/j.icheatmasstransfer.2017.02.016.

[27] Zhao Z-L, Zhou S, Cai K, Xie YM. A direct approach to controlling the topology in structural optimization. Comput Struct 2020;227:106141. https://doi.org/10.1016/j.compstruc.2019.106141.

[28] Zhao Z-L, Zhou S, Feng X-Q, Xie YM. On the internal architecture of emergent plants. J Mech Phys Solids 2018;119:224–39. https://doi.org/10.1016/j.jmps.2018.06.014.

[29] Audibert C, Chaves-Jacob J, Linares J-M, Lopez Q-A. Bio-inspired method based on bone architecture to optimize the structure of mechanical workspieces. Mater Des 2018;160:708–17. https://doi.org/10.1016/j.matdes.2018.10.013.

[30] Lin S, Bao DW, Xiong CW, Fang J, An HW, et al. Human-made corals for marine habitats: Design optimization and additive manufacturing. Adv Eng Softw 2021;162–163:103065. https://doi.org/10.1016/j.advengsoft.2021.103065.

[31] Lowe RJ, Falter JL. Oceanic forcing of coral reefs. Ann Rev Mar 2015;7:43–66. https://doi.org/10.1146/annurev-marine-010814-015834.

[32] Fentimen R, Lim A, Rüggeberg A, Wheeler AJ, Van Rooij D, Foubert A. Impact of bottom water currents on benthic foraminiferal assemblages in a cold-water coral environment: The moira mounds (ne atlantic). Mar Micropaleontol 2020;154:101799. https://doi.org/10.1016/j.marmicro.2019.101799.

[33] Baldock TE, Karampour H, Sleep R, Vyltla A, Albermani F, Golshani A, et al. Resilience of branching and massive corals to wave loading under sea level rise - a coupled computational fluid dynamics-structural analysis. Mar Pollut Bull 2014;86:91–101. https://doi.org/10.1016/j.marpolbul.2014.07.038.

[34] Wen H, Ren B, Dong P, Zhu G. Numerical analysis of wave-induced current within the inhomogeneous coral reef using a refined sph model. Coast Eng 2020;156:103616. https://doi.org/10.1016/j.coastaleng.2019.103616.

[35] Stocking JB, Laforsch C, Sigl R, Reidenbach MA. The role of turbulent hydrodynamics and surface morphology on heat and mass transfer in corals. J Roy Soc Interface 2018;15. https://doi.org/10.1098/rsif.2018.0448.

[36] Lohan D, Dede E, Allison J. Topology optimization for heat conduction using generative design algorithms. Struct Multidiscip Optim 2017;55:1063–77. https://doi.org/10.1007/s00158-016-1563-6.

[37] Guest JK. Imposing maximum length scale in topology optimization. Struct Multidiscip Optim 2009;37:463–73. https://doi.org/10.1007/s00158-008-0250-7.

[38] Krüger T, Kusumaatmaja H, Kuzmin A, Shardt O, Silva G, Viggen EM. The Lattice Boltzmann Method - Principles and Practice. Springer; 2016. https://doi.org/10.1007/978-3-319-44649-3.

[39] Krivovichev GV. Linear bhatnagar-gross-krook equations for simulation of linear diffusion equation by lattice boltzmann method. Appl Math Comput 2018;325:102–19. https://doi.org/10.1016/j.amc.2017.12.027.

[40] Silva G. Discrete effects on the forcing term for the lattice boltzmann modeling of steady hydrodynamics. Comput Fluids 2020;203:104537. https://doi.org/10.1016/j.compfluid.2020.104537.

[41] Chu Y, Wang A, Zhu Y, Wang H, Liu K, Ma R, et al. Enhancing the performance of basic magnesium sulfate cement-based coral aggregate concrete through gradient composite design technology. Compos Part B: Eng 2021;227:109382. https://doi.org/10.1016/j.compositesb.2021.109382.